Chapter II

Synthesis and characterization of different forms of tungsten disulphide nanosystems

2.1 Synthesis routes and physical characterization techniques employed

Synthesis of quality nanomaterials has always been a topic of experimental research to cater industrial needs and subsequent relevance research. While synthesizing nanomaterials, cost effectiveness, quality, scale of production, feasibility etc. are the points which are taken into consideration quite actively. Obtaining micro and nano-scale WS_2 systems was not easy due to lack of availability of standard, cost-effective and user-friendly routes in spite of numerous efforts made in the past. Earlier, nanoscale WS_2 systems were synthesized using methods, such as, chemical vapour deposition [1], magnetron sputtering [2], laser ablation [3], etc., all of which come with much sophistication and with a need for high temperature. Synthesizing nanoscale WS_2 *via* a hydrothermal route does not require very high temperature processing and could offer products with less or no agglomeration, phase homogeneity and good crystallization [4]. The present chapter focuses on the approaches adopted to synthesize WS_2 nanosystem of different morphologies. The structural, optical and morphological features of the synthesized nanosystems are also discussed.

To exploit the structural and crystallographic properties, X-ray diffraction (XRD) technique was employed using a MiniFlex Rigaku X-ray diffractometer equipped with a CuK_α source (λ= 1.543 Å). The morphological details of the as-synthesized WS_2 samples were revealed through the scanning electron microscopy (JEOL, 6390LV) and transmission electron microscopy (FEI, Tecnai) imaging studies. The elemental composition of the samples is predicted through the EDX spectra. On the other hand, luminescence characteristics and phonon-assisted vibrational modes are exploited through the luminescence spectrophotometer (Hitachi 2700 FL) and Raman spectrometer (Renishaw, Wottonunder-Edge); respectively. The optical absorption responses as obtained from the UV–Vis spectroscopy (UV 2450, Shimadzu Corporation) studies have been used for estimating energy band gaps. Information regarding nanosheet-surface area, pore size and pore distribution were evaluated through the Bruner–Emmet–Teller (BET, Quantachrome Nova 1000e, FL) analysis performed on the

WS_2 nanosheets by way of studying N_2 adsorption/desorption characteristics at liquid nitrogen temperature (~77 K).

2.2 Inorganic fullerene (IF) type - WS_2 nanoparticles

2.2.1 Hydrothermal synthesis

We have attempted a two-step hydrothermal process for the production of nano-WS_2. The chemicals used in the synthesis were of analytical grade and used without further purification. While sodium tungstate ($Na_2WO_4.2H_2O$) (Rankem, 98% pure) was considered as the source of tungsten, thiourea (CH_4N_2S) (Merck, 99% pure) as the source of sulphur. First, 1.64 g of sodium tungstate, 0.69 g of hydroxylamine hydrochloride (NH_2OH_2Cl) (Merck, 98% pure) and 1.52 g of thiourea are dissolved in 30 ml of deionized Millipore® water. The mixture was kept under constant stirring for 25 min, with the pH value adjusted to 6 by adding a few drops of ammonia water. The solution is transferred to a 50-ml teflon-lined stainless steel autoclave, which was properly sealed and then subjected to oven heating at a temperature of 180 ^{0}C, for 24 h. The collected product is washed several times with distilled water and then with ethanol under centrifugation (3500 rpm) for about 15 min. The precipitate obtained is oven dried at a temperature of 60 ^{0}C, for 10 h. The resultant product that appeared to be blonde yellow in colour is labeled as S_1. The obtained light

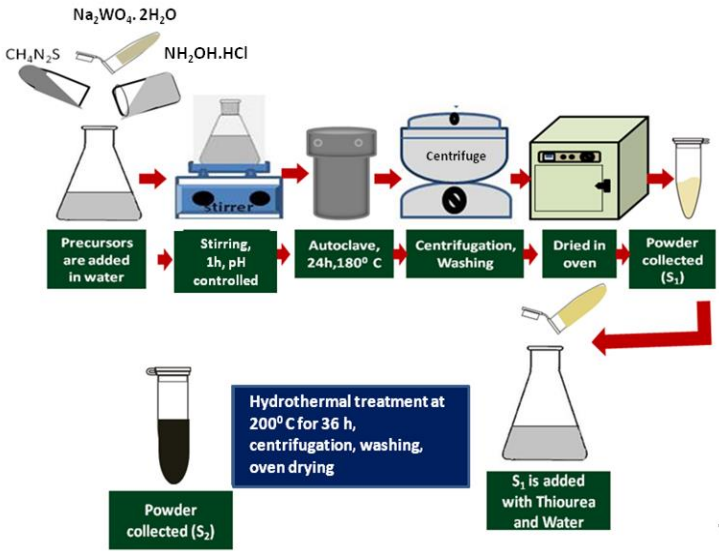

Figure 2.1: Schematic diagram of synthesis of IF-type WS_2 nanoparticles.

coloured powder resembles that of an intermediate product (WO_{3-x}) in the formation of WS_2 which may arise due to the inadequacy of sulphur in the reaction process [4].

In the second step, 0.58 g of *S1* (obtained through the first step) is mixed with 0.78 g of thiourea and 40 ml deionized water in a conical flask and subjected to vigorous stirring for about 20 min. Then, the solution is poured in a 50-ml teflon-lined stainless steel autoclave, sealed airtight and kept in an oven maintained at a temperature of 200 ^{0}C, for 36 h. The product is centrifuged (3500 rpm, 5 min), washed with distilled water and finally, cleansed with ethanol suitably. The product is then dried in an oven (80 ^{0}C) for about 10 h. The steps as regards formation of the final nano-WS_2 product (*S2*) are illustrated in Fig. 2.1. The chemical equations involved are as given below [4]:

$$CS(NH_2)_2\ (s) + 2H_2O(l) \longrightarrow H_2S\ (g) + CO_2\ (g) \qquad (2.1)$$

$$WO_{3-x} + H_2S + H_2O \longrightarrow WO_2 + SO_4^{2-} + H^+ \qquad (2.2)$$

$$WO_2(s) + H_2S\ (g) \longrightarrow WS_2\ (s) + H_2O\ (l) \qquad (2.3)$$

2.2.2. Structural and morphological characteristics of IF-WS_2

The XRD patterns of the as-prepared samples are shown in Fig. 2.2 (a, b). It can be seen that the sample *S1* exhibits diffraction peaks which is similar to that of $WO_3.5H_2O$ (JCPDS File No. 44-0363) and $WO_3.33H_2O$ (JCPDS File No. 35-1001) [4]. Attributed to (002) plane of hexagonal WS_2, the diffraction peak at 2θ ~15.20^0 in sample *S1* is marginally shifted to 14.32^0 as in system *S2* (JCPDS File No.08-0237) [4]. The other peaks at 28.76^0, 33.4^0, 39.57^0, 44.28^0, 49.65^0 and 58.53^0 corresponded to (004), (101), (103), (006), (105) and (110) planes of the hexagonal WS_2, respectively. The sharp peaks corresponding to the (002) and (103) planes suggest competitive growth of the crystallites along these directions. The sharp diffraction lines are also shown in the figure in accordance with the respective JCPDS files. From the analyses of diffractograms, it is quite apparent that the

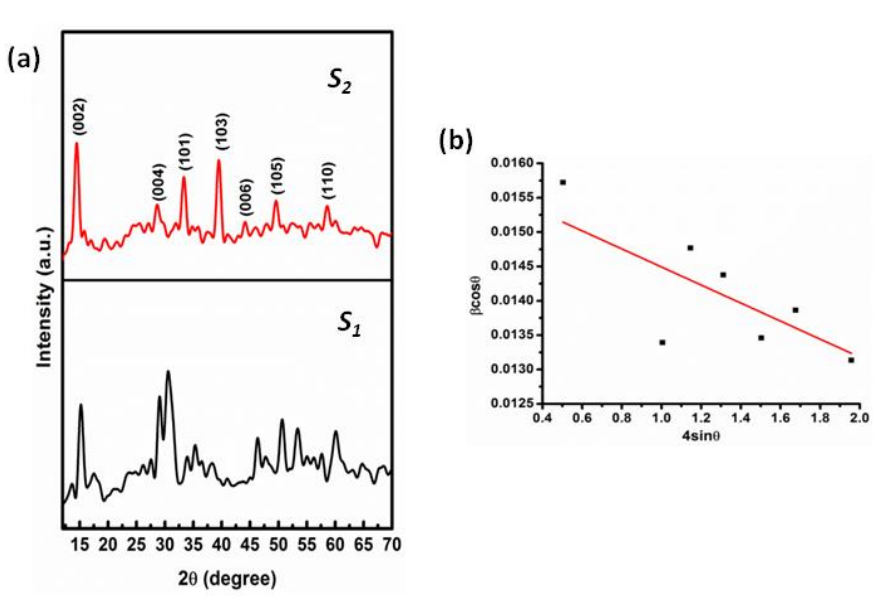

Figure 2.2 (a): X-ray diffractograms of the prepared samples, and (b) the W-H plot for sample S_2.

synthesized product obtained through the additional step ensured the desired phase of the nano-WS_2 system. The average crystallite size (D) of the WS_2 nanoparticles was calculated using the Williamson–Hall (W-H) plot by choosing the most prominent diffraction peaks, such as (004), (101), (103), (006), (105) and (110). The W-H expression is given by:

$$\beta \cos\theta = 4\boldsymbol{\varepsilon} \sin\theta + \frac{0.9\lambda}{D} \qquad (2.4)$$

where $\boldsymbol{\lambda}$ is the wavelength of the X-ray radiation ($\boldsymbol{\lambda}$ = 1.543 Å for CuK_α line), 2θ is the diffraction angle, β is the line width at half maximum height and $\boldsymbol{\varepsilon}$ is the mean lattice strain. As can be found in Fig. 2.2 (b), by plotting $\beta cos\theta$ vs. 4 $sin\theta$, the size component can be obtained directly from the intercept of the straight line, on the y-axis [5].

Similarly, microstrain $\boldsymbol{\varepsilon}$ can be evaluated from the desired slope. Using the W-H formula, the average crystallite size was calculated to be ~7.7 nm and the microstrain as, -1.3×10^{-3}. The negative strain corresponds to the relaxed nature of the crystallites, whereas positive strain indicates compaction of the crystallites [6]. Using conditions relevant to the hexagonal structure, the crystal lattice parameters can be found as, $a = b$ = 3.16 Å and c = 12.28 Å.

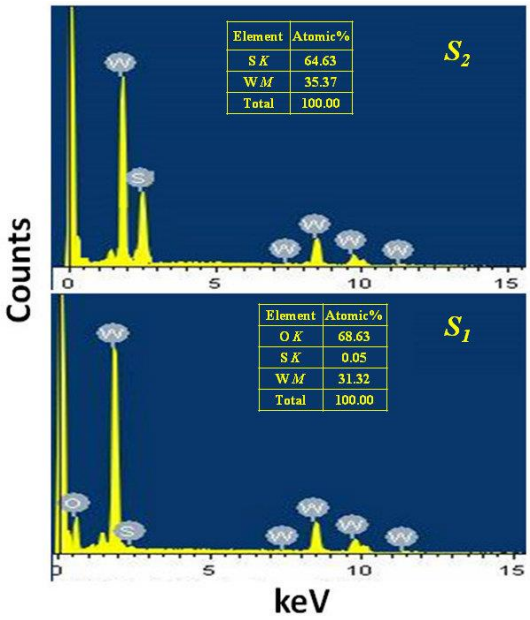

Figure 2.3: EDX spectra of the as-prepared nano-WS_2 samples

The EDX spectra of the two samples S_1 and S_2 are shown in Fig. 2.3. The presence of elements W, O and S is quite evident from the EDX spectrum of S_1. However, the amount of sulphur present in sample S_1 is quite small. The amount of sulphur present is significantly high in sample S_2, as compared to S_1. Since no oxygen peak is witnessed in the EDX spectrum of sample S_2, it substantiates the development of high-yield WS_2 phase, free from the oxide content. Moreover, the sample S_2 gave the atomic ratio of W to S as, 1:1.83. Since the formation of phase-pure WS_2 is ascertained, further characterization wrt imaging was considered for the sample S_2.

Fig. 2.4 shows the SEM micrographs of the desired WS_2 nanosystem. Here, we could notice clearly the formation of clustered nanoparticles, similar to an earlier work [7]. It is worth mentioning here that, the structural morphology of the WS_2 nanostructures is largely dependent on the reaction time and processing temperature [8]. The agglomeration of particles is caused due to the multi-nuclei attachment, which serves as the possible mechanism of growth along (002) direction [9]. The low and high magnification micrographs are shown in Fig. 2.4 (a) and (b); respectively.

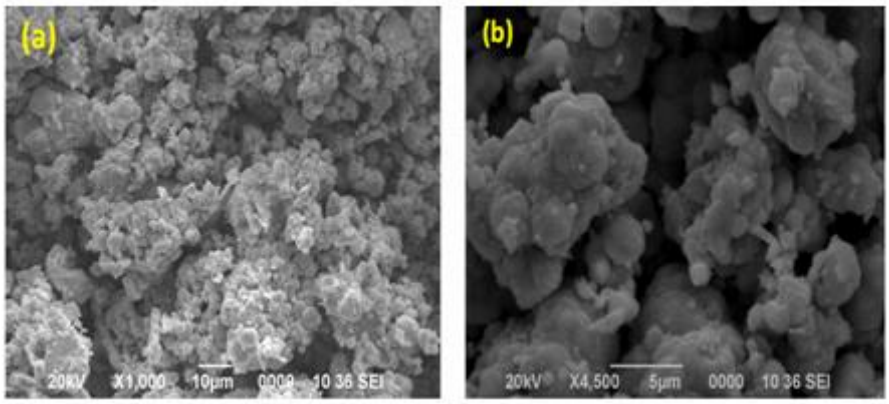

Figure 2.4: SEM micrographs of the as-prepared nano-WS_2 system: (a) low magnification, (b) high magnification.

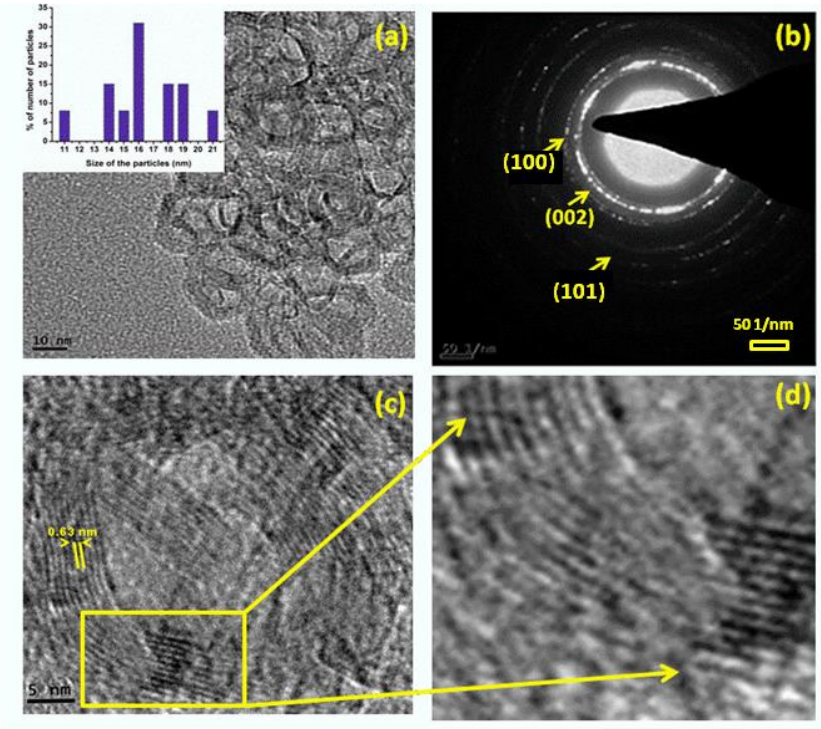

Figure 2.5 (a): TEM micrograph depicting distributed view of IF-type WS_2 nanoparticles with a histogram on size distribution (inset), (b) SAED pattern, (c) a single IF nano-WS_2 structure and (d) enlarged view of a segment showing the bent lattice structure of the WS_2 nanosystem.

Fig. 2.5 (a–d) depicts a series of TEM imaging features of the nano-WS_2 system. Apparently, the TEM image reveals the development of fullerene-shaped structures of the nano-WS_2 system (Fig. 2.5 (a), (c)). The size distribution is show

shown in the inset of Fig. 2.5 (a). The formation of diffused rings as witnessed in the SAED micrograph (Fig. 2.5 (b)) suggests the polycrystalline nature of the synthesized product which could arise due to the presence of surface defects on the nano-WS_2 system [10]. The hollow core IF -type structures with bent lattice edges can be found in Fig. 2.5 (c). In the magnified image of the corner of an individual IF structure we noticed that a corner is essentially formed from a series of bent lattice planes (Fig. 2.5 (d)). In this regard, strain relief mechanism has been proposed in support of exhibition of such an unusual morphology/structure [11].The average outer diameter of the IF nano-WS_2 particles is estimated to be ~16 nm, with an interlayer spacing of 0.63 nm.

2.2.3 Optical and spectroscopic properties

Fig. 2.6 represents the Raman spectrum of the synthesized nano-WS_2 system acquired at an excitation wavelength, λ_{ex} ~514 nm. Raman spectroscopy is a noninvasive, yet important tool to reveal structural information as regards number of layers, defects, doping levels, strain effects and other factors. In fact, bulk WS_2 shows two major bands corresponding to E^1_{2g} and A_{1g} modes located at ~351 and 420 cm^{-1}, respectively [12]. In our case, the two vibronic bands are witnessed at ~352 and 420 cm^{-1} which corresponded to the first-order modes at

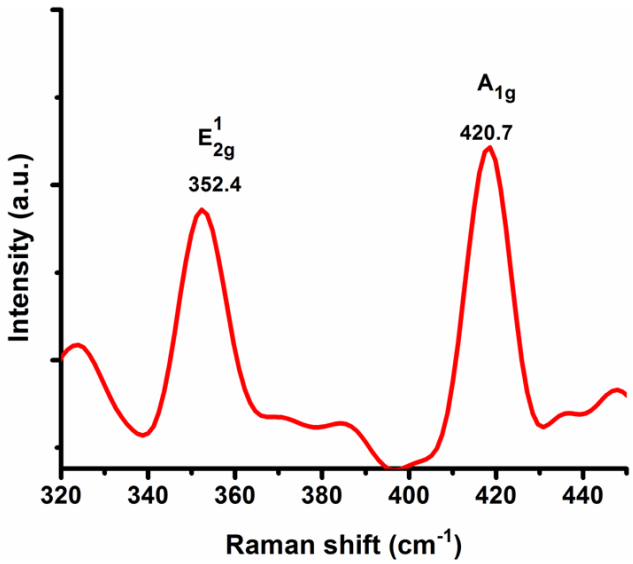

Figure 2.6: Raman spectrum of the as-prepared IF-type WS_2 nanosystem (S_2).

the Brillouin zone; with first being an in-plane mode E^1_{2g} and the second identified as out-of-plane mode, A_{1g} [13]. These values are slightly different when compared to those of the bulk WS_2 crystal. A slight shifting of A_{1g} mode towards higher wavelength side may be due to the decrease in the interlayer Van der Waals interaction which causes weakened restoring forces in the vibration as we move from the bulk to a few layer system of WS_2 [14].

On the other hand, the blue shift in E^1_{2g} is attributed to the reduced long-range Coulomb interaction between the effective charges caused by an increase in the dielectric screening on stacking-induced changes in the interlayer bonding [14]. The ratio of intensities of the E^1_{2g} and A_{1g} calculated stands at 0.61 which is higher than that of bulk WS_2 but lower than the mono, bi and tri-layered WS_2 nanosystems [15]. Thus our IF-type nano-WS_2 must comprise sufficient number of layers, which results in a dominant out-of-plane vibration over the in-plane one.

The FTIR spectroscopy essentially offers information regarding the nature of chemical bonding and the molecular structure of the system under study. Fig. 2.7 depicts the FTIR spectrum of the synthesized nano-WS_2 system in the wavenumber range 400–3200 cm^{-1}. A distinct band at ~454 cm^{-1} refers to the characteristic S–S bond of the elemental sulphur [16]. The bands positioned at ~580.2 and 978.6 cm^{-1} are ascribed to the W-S bond and S–S bond, respectively [17]. The bands found at ~1403.3 and 1625.5 cm^{-1} are ascribed to the stretching vibrations of the hydroxyl group [17]. Moreover, the vibrational bands at 2895.7 and 2924 cm^{-1} can be attributed to the atmospheric OH available during experiment of the WS_2 system [17].

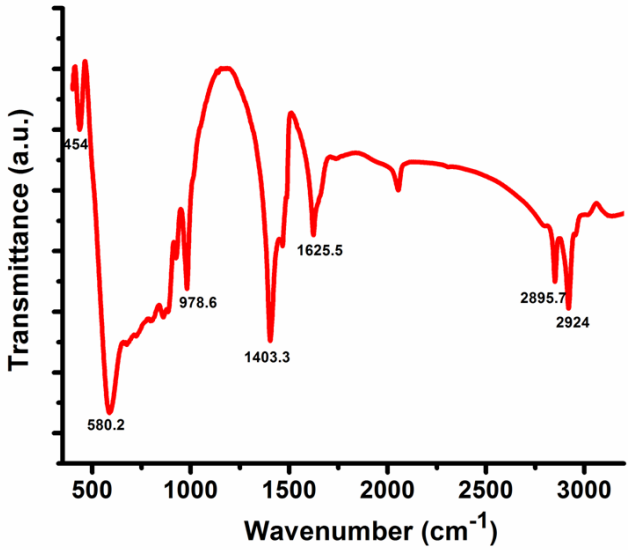

Figure 2.7: FTIR spectrum of the as-prepared IF-type WS_2 nanosystem (S_2).

The UV–Vis optical absorption spectrum of the nano-WS_2 is shown in Fig. 2.8(a). It depicts presence of two weak absorption bands located at ~537 and 649 nm. Even though these two bands represent characteristic absorption response of the IF-WS_2 nanostructures [18, 19], particularly the latter peak corresponds to *d–d* type transitions of the WS_2 at the center of the Brillouin zone [20].

To determine the band gap of the prepared WS_2 nanoparticles, we have plotted the Tauc's plot using the relation [17], $\alpha h\nu = (h\nu - Eg)^n$, where h is the Planck's constant, ν is the frequency of the incident light and α is the absorption coefficient. Putting $n = 1/2$ for the direct allowed transitions, the band gap of the prepared WS_2 nanosystem is estimated to be 1.91 eV, which is in good agreement with the earlier report [21].

PL is a versatile tool to exploit the radiative emission and defect-mediated transitions. PL spectroscopy study is necessary to understand the carrier recombination processes to be understood for photocatalysis in latter studies.

Fig. 2.8(b) shows the PL spectrum of the synthesized WS_2 nanosystem acquired under an excitation wavelength of λ_{ex} = 460 nm. The broad peak at ~638 nm is

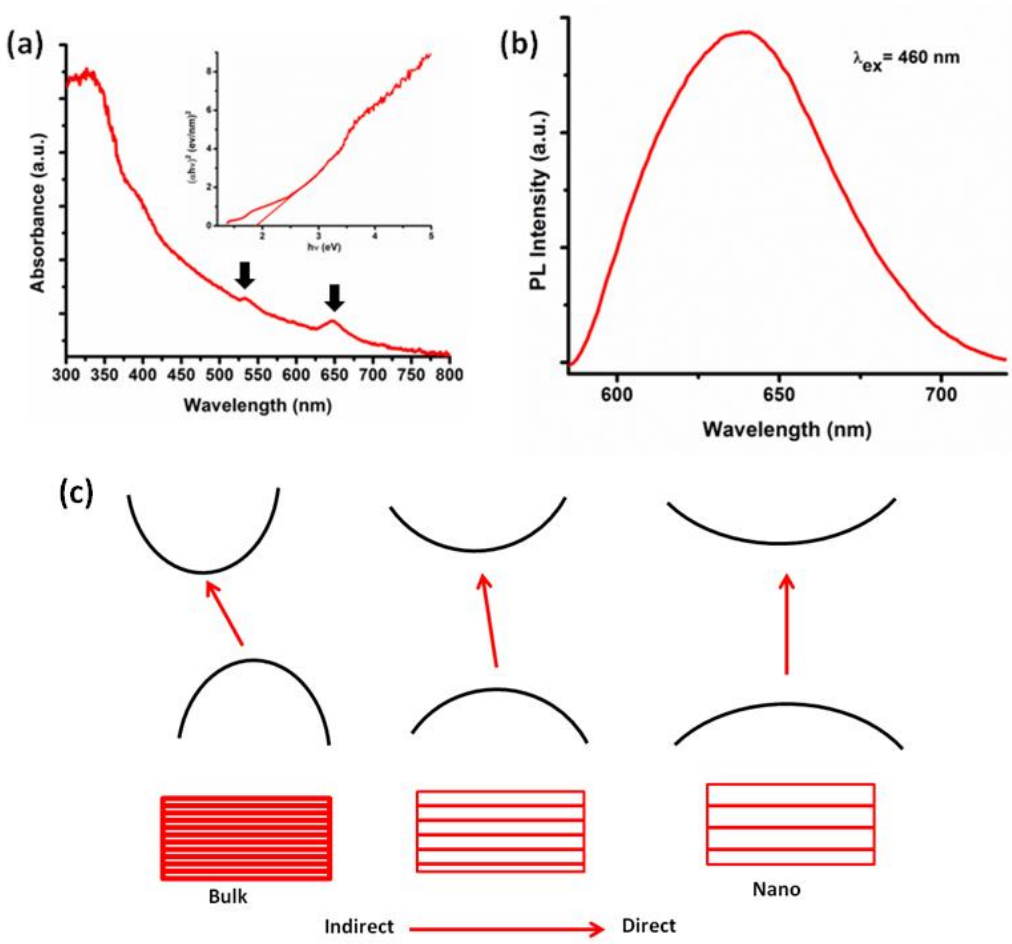

Figure 2.8 (a): UV–Vis optical absorption spectrum along with the Tauc's plot (inset) (b) PL spectrum of the IF nano-WS_2 system (c) Schematic diagram showing indirect to direct band gap transition.

the outcome of transition from the indirect band gap type to the direct band gap one when the bulk system is thinned down to a few nanometric layers [14]. This peak suggests the separation efficiency of the electron–hole pairs, with superior characteristics due to the presence of surface area and active edges [22]. Reports suggest that a direct gap exists at the K points of the Brillouin zone between the spin-orbit split valence band and the doubly degenerate conduction band. The indirect band gap is known to form between a local conduction band, which is minimum at the midpoint between Γ and K valley and the valence band, maximum at the Γ point [14]. The existence of the direct transition can be

explained from excitonic radiative relaxation and accordingly, the appearance of PL peak has been observed at energies slightly lower than the 2.05 eV direct band gap of WS_2 [14]. The luminescence pattern is observed to be asymmetrically broadened and with a fullwidth half-maxima (FWHM) of approximately, 183 meV. A broad emission peak suggests that, the transition from indirect to direct nature of the gap is not discrete, but continuous over an inseparable energy band.

2.3 WS_2 nanosheets

2.3.1 Hydrothermal synthesis cum exfoliation

At first, a single-step hydrothermal process is attempted for the production of WS_2 powder and then, exfoliated into its nanosheet form with the help of repeated ultrasonication. The chemicals used in the synthesis were of analytical grade and were used without further purification. For synthesis, sodium tungstate ($Na_2WO_4.2H_2O$) (Rankem, 98% pure) was used as the source of tungsten, and thiourea (CH_4N_2S) (Merck, 99% pure) as for sulphur. In a typical synthesis, 1.65 g of sodium tungstate, 0.72 g of hydroxylamine hydrochloride ($NH_2OH.HCl$) (Merck, 98% pure) and 1.17 g of thiourea were dissolved in 30 ml of deionized Millipore® water. The solution was stirred for 1 h until a clear solution is obtained, while maintaining the solution at pH=6. The mixture was then transferred into a 50 ml teflon-lined autoclave, and upon proper sealing, it was kept in the oven at a temperature of 200 ^{0}C for 24 h. After allowing it to cool naturally, the obtained product was washed several times with deionized water and ethanol and then centrifugation (~4000 rpm) was employed for about 10 min. The precipitate was oven-dried at a temperature of 60 ◦C and consequently, a dark grey-coloured powder has been acquired. The synthesized powder was labeled as S_1.

In order to obtain nanosheets out of the synthesized WS_2 powder, 0.2 g of the powder was added to 20 ml of 1-methyl-2-pyrolidone (Merck, 99.5% pure) and

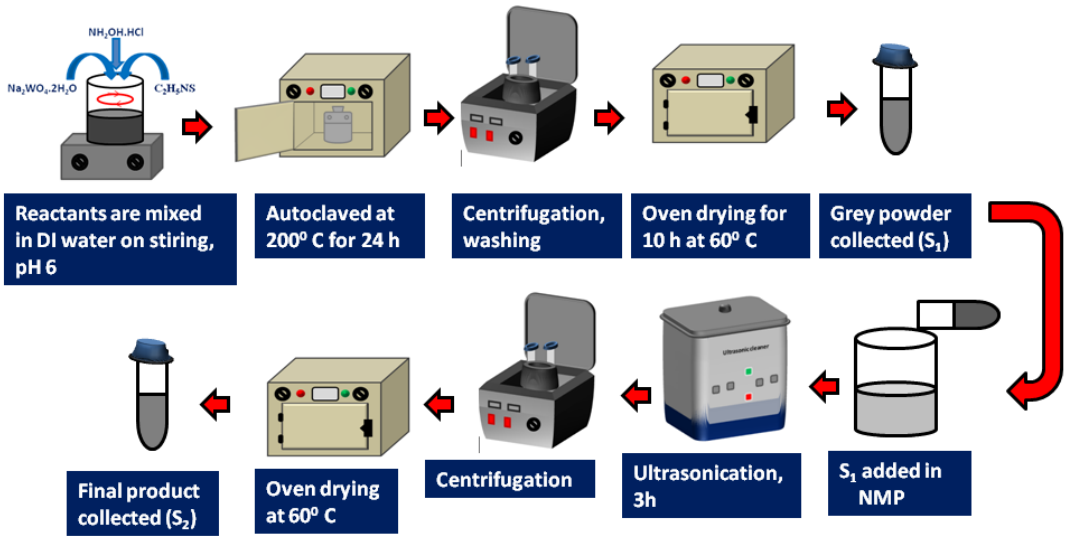

Figure 2.9: Representative steps as regards the synthesis of WS_2 nanosheets.

then, subjected to ultrasonication bath (UD100SH: f = 50 Hz, P = 100 W) for 4 h. The solution was then adequately centrifuged (~5000 rpm) for 10 min after which two-third of the solution was considered for further centrifugation (~7000 rpm) for 15 min. This was followed by multiple washing with ethanol. The as-received precipitate was collected and subsequently oven-dried (~60 ◦C), for a time duration of ~10 h. The resulting product, which yielded WS_2 nanosheets, was labelled as S_2. The whole synthesis steps are highlighted in a block diagram shown in Fig. 2.9

2.3.2 Structural and morphological characteristics

Fig. 2.10 shows the XRD patterns of the as-prepared WS_2 samples (un-exfoliated and nanosheets). The samples exhibit diffraction peaks at nearly same positions and no shift in the peak position was observed. The diffraction peaks positioned at 2θ = 28.76, 32.66, 33.42, 35.26, 39.57, 44.28, 49.65, 55.53 and 60.31 which corresponded to (004), (100), (101), (102), (103), (006), (105), (106) and (008) planes of the hexagonal (H) structure of WS_2, respectively [4]. The prominent peak located at 2θ = 14.38◦ signifies the (002) plane of 2H-WS_2 (JCPDS file no. 08-0237). The remarkable difference between the XRD patterns
of the two samples is in the intensity of the peaks, with the nanosheets possessing a relatively lower strength due to lack of adequate atomic planes

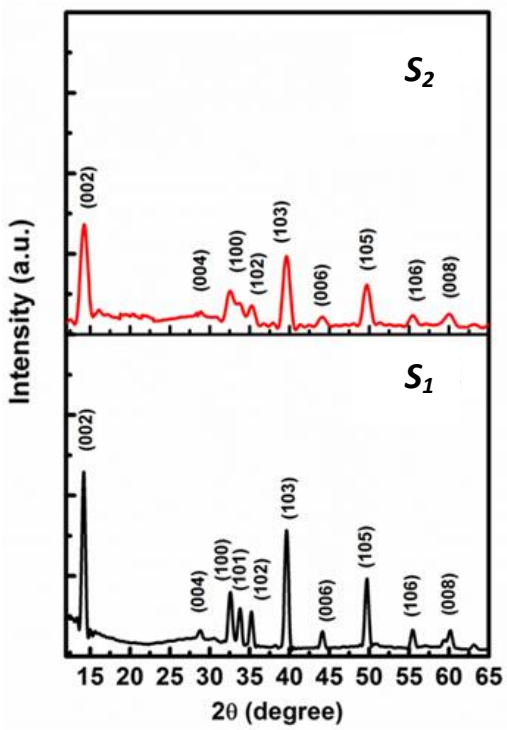

Figure 2.10: XRD patterns of un-exfoliated WS_2 (S_1) and exfoliated WS_2 nanosheets (S_2).

participating in the diffraction process. The lowering of the peak intensity is attributed to the decrease in crystallinity of the nanosheet as compared to the un-exfoliated WS_2 powder [23]. The diffraction peaks of WS_2 sheets also tend to get broadened, and which suggests the exfoliation of the WS_2 powder into the sheets of nanoscale form [24]. No peak due either to impurities or oxide phase was witnessed in the diffractograms, thus indicating formation of the phase-pure WS_2 product in this case.

The micrographs of the un-exfoliated (S_1) and nanosheet (S_2) WS_2 powder captured on a HRSEM machine are shown in Fig. 2.11 (a) and (b), respectively. Fig. 2.11(c) shows the EDX micrograph of the as-synthesized WS_2 powder. The presence of the elements W and S can be clearly seen in the EDX spectrum. Intensity-based calculations gave the ratio of S to W to be 1.90:1. A lowered sulphur content in the system could lead to the presence of numerous of sulphur vacancies in the WS_2 specimen under study.

.

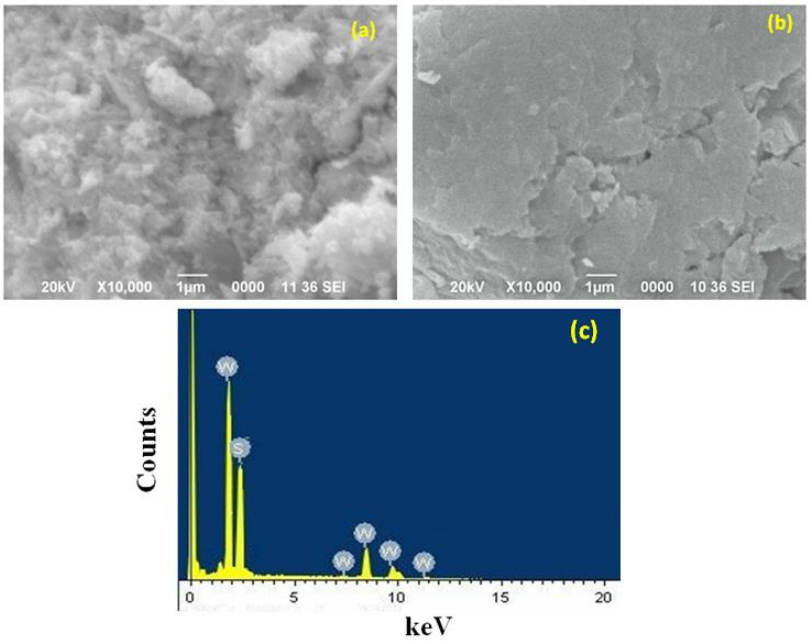

Figure 2.11: SEM micrograph of (a) un-exfoliated WS_2 powder and (b) exfoliated WS_2 nanosheets; (**c**) The EDX micrograph of the un-exfoliated WS_2 powder.

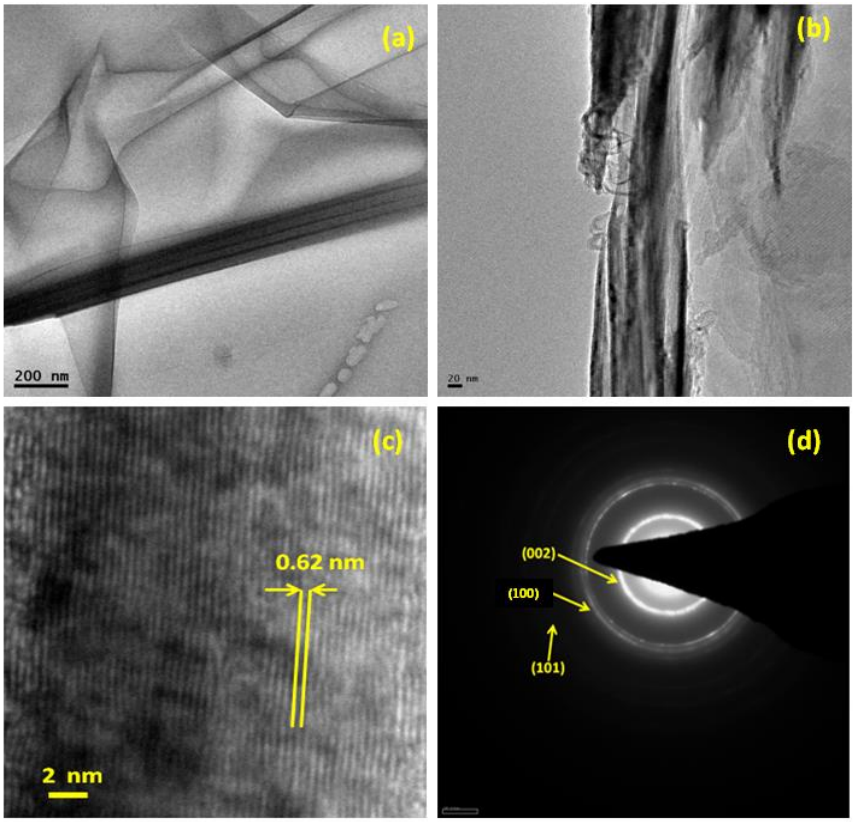

Figure 2.12: TEM micrograph of (a) WS_2 nanosheets, (b) magnified view of the sheets, (c) lattice fringe pattern captured at the surface and (d) SAED pattern indicating diffused diffraction rings.

Moreover, the exfoliated sheets are visualized at a low and high magnifications through TEM imaging ((Fig. 2.12 (a,b)). The nanosheets indicating a higher surface area coverage can be noticed with the evidence of kinks and folds. The lattice fringe pattern captured at the edge of the WS_2 nanosheets is shown in Fig. 2.12 (c). Using *ImageJ*® software [25], the average fringe width defining lattice spacing of the nanosheets was calculated to be ~0.62 nm. Moreover, the observation of diffused ring like patterns is an indicative of the polycrystalline content present in the synthesized WS_2 product ((Fig. 2.12 (d)).

2.3.3 Optical and spectroscopic characteristics

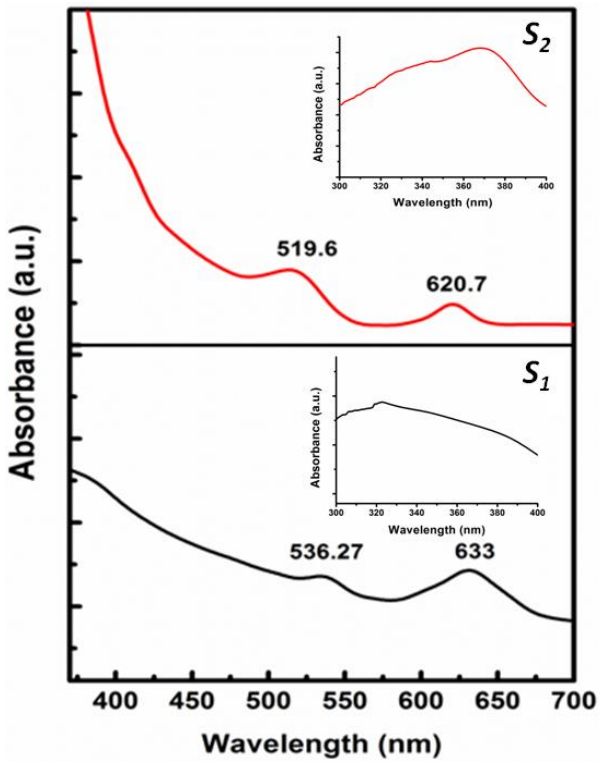

Figure 2.13: UV–Vis optical absorption spectra of the un-exfoliated WS_2 powder (S_1) and exfoliated WS_2 nanosheets (S_2).

In the optical absorption spectra shown in Fig. 2.13, two absorption peaks located at 536 and 633 nm can be observed for the un-exfoliated WS_2 system (S_1). The absorption peak at 536 nm is ascribed to the transitions from spin-splitted valence band to the conduction band [26], whereas the peak at 633 nm corresponds to *d*–*d* type transitions at the centre of the Brillouin zone [27]. The corresponding peaks are blue-shifted to 519.6 and 620.7 nm on exfoliation as witnessed for the nanosheets (S_2). Earlier, the blue-shifting of the absorption peaks was viewed as a consequence of quantum confinement effect [27]. Consequently, here the optical band gap would increase for the exfoliated WS_2 nanosheets, as compared to its un-exfoliated form. Moreover, the second peak is effectively suppressed for the nanosheets owing to a lowered value of *d*–*d* transition probability.

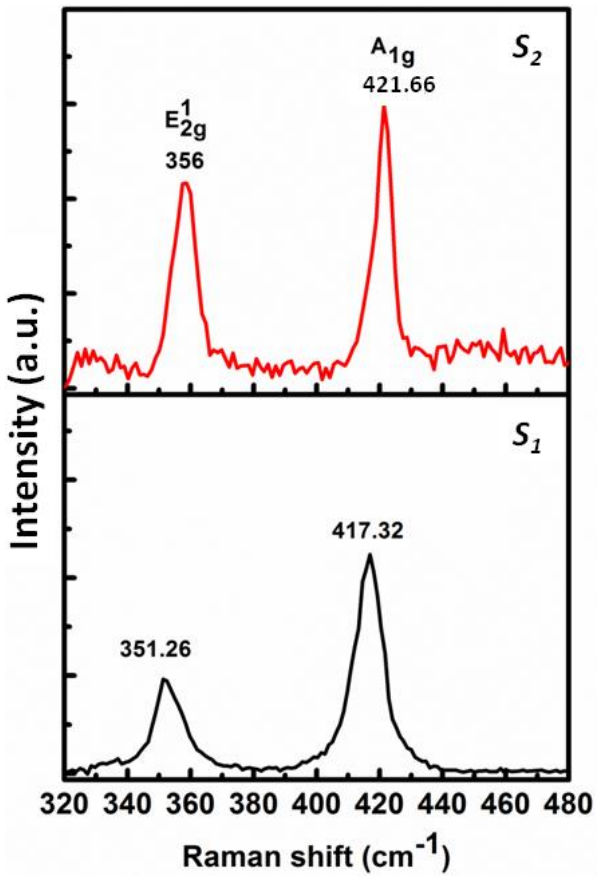

Figure 2.14: Raman spectra of the un-exfoliated WS_2 nanopowder (S_1) and exfoliated WS_2 nanosheets (S_2).

Fig. 2.14 highlights the Raman spectra of the as synthesized WS_2 systems. Apparently, two distinct peaks corresponding to the E^1_{2g} and A_{1g} Raman active modes can be seen [28]. The E^1_{2g} mode represents an in-plane optical mode, whereas the A_{1g} mode signifies the out-of-plane vibrations of the sulphur atoms [29]. We also noticed a small blue-shifting in the Raman peaks from 351.26 (417.32) to 356.07 (421.66) cm^{-1}, as S_1 was converted to S_2 through exfoliation. The exfoliation causes a weak layer interaction, leading to an appreciable peak shifting towards a higher wavenumber [30]. The ratio of the intensities of the E^1_{2g} and A_{1g} peaks was calculated to be 0.68 for the nanosheets, which is comparatively higher than the bulk WS_2 [31]. Owing to the phonon confinement effect, a blue shifting of the Raman peaks could be noticed in case of the WS_2 nanosheets as compared to the un-exfoliated form.

2.3.4 N_2 adsorption–desorption features:

Surface analysis of nanoscale materials is an important aspect as it offers sound information regarding surface coverage and particularly, specific surface area, pore size, pore volume, etc. In this regard, earlier N_2 adsorption and desorption

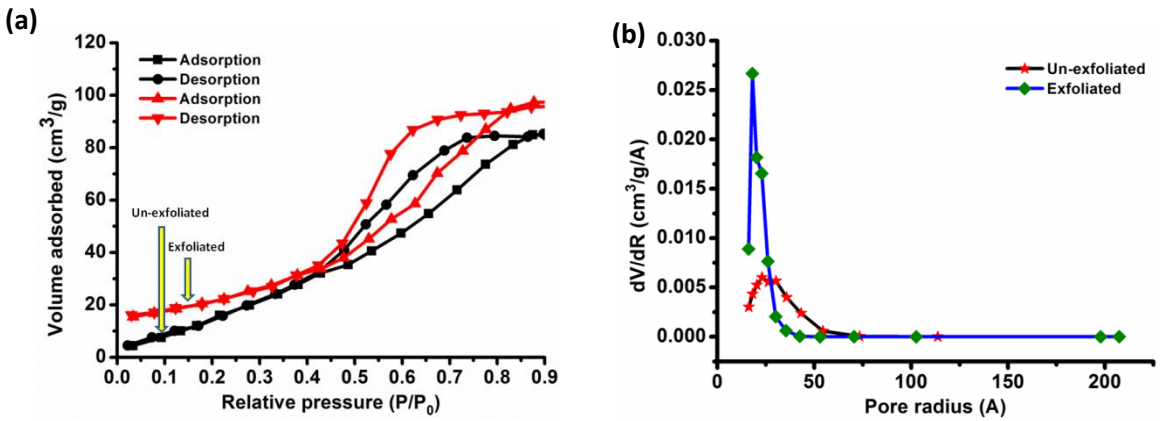

Figure 2.15 (a): The nitrogen gas adsorption–desorption curve and (b) The BJH pore size distribution curve of the unexfoliated WS_2 and WS_2 nanosheets.

isotherms were employed for studying mesoporous WS_2 [17]. The type of isotherm is identified as type IV profile, which is the characteristic of a mesoporous material with pore diameter typically in the range of 2–50 nm [32]. Essentially, adsorption on mesoporous solids occurs *via* multilayer adsorption phenomena mediated *via* capillary condensation that results in type IV and V isotherms [33]. Here, Fig. 2.15 represents the characteristic N_2 adsorption/desorption isotherms of our hydrothermally processed un-exfoliated WS_2 powder and exfoliated WS_2 nanosheets. The initial part of the type IV isotherm is attributed to monolayer–multilayer adsorption, since it follows the same trend as the corresponding part of a type-II isotherm obtained with the given adsorptive on the same surface area of the adsorbent in a nonporous form. The hysteresis loop is appeared to be of the type H2 according to IUPAC classification, which indicates disordered distribution of pore size and shape. The hysteresis loop is found to occur at a magnitude above ~0.5 of relative pressure, P/P_0. The BJH pore-size distribution graph for the same samples is shown in the inset of Fig. 2.15. The BET surface area of the nanosheets is found to be 211.5 m^2g^{-1} whereas it is 120.1 m^2g^{-1} for the WS_2 nanopowder. Using the BJH model, the pore volume and the average size of the pores of the WS_2 nanosheets are estimated to be 0.433 cc g^{-1} and 3.8 nm, respectively. On the other hand the pore volume and the average pore size of the un-exfoliated nanopowder is obtained as, 0.145 cc g^{-1} and 4.6 nm; respectively.

The Kelvin's equation [34] is:

$$\ln \frac{P}{P_0} + \frac{4\gamma V_m}{dRT} = 0 \qquad (2.5)$$

where P and P_0 represent actual and saturated vapor pressures, V_m is the molar volume, γ is the surface tension of liquid N_2 and d (=2r, r being radius) is the size of the droplet. The symbols R and T signify universal gas constant (8.31 J-Mol^{-1} K^{-1}) and working temperature (77 K); respectively. Putting the respective values, we obtain the respective diameters of the drop that desorb out of the pores as, d=2r=2.1 nm and 2.2 nm as for the WS_2 nanosheets and un-exfoliated

nanopowder. However, a relatively larger pore sizes (2*r* ~3.8 and 4.6 nm) predicted through the experimental analysis (Fig. 2.15 (b)), might have arisen due to the existence of interconnected pores on the surfaces of the nanosheets and the nanopowder of WS_2.

2.4 WS_2/C-dot nanohybrid systems

2.4.1 Synthesis from powder to 2D and nano-hybrid systems

A facile, hydrothermal route has been employed for the production of WS_2 nanopowder. In a typical experiment, 1.65 g of sodium tungstate ($Na_2WO_4 \cdot 2H_2O$; Rankem, 98% pure), and 1.52 g of thiourea (CH_4N_2S; Merck, 99% pure) were dissolved in 30 ml of deionized (DI) water. Latter, 0.72 g of hydroxylamine hydrochloride ($NH_2OH.HCl$; Merck, 98% pure) is added to the aforesaid solution. The mixture was kept under constant stirring (~300 rpm) for about 1 h, with pH adjusted to 6 by dropping a few ml of dilute hydrochloric acid (HCl). The sol was then transferred into a 50 ml teflon-lined stainless steel autoclave, sealed properly and latter placed in an open air oven at a temperature of 200 °C, for 24 h. The autoclaved product was collected and then washed several times with DI water and with the AR grade ethanol under high speed centrifugation (~10,000 rpm). The residue was then dried in vacuum oven kept at a temperature of 70 °C, for 10 h. The obtained product ensured a bluish grey appearance.

The as-prepared WS_2 nanopowder is converted to 2D sheets via ultrasonication. At first, 0.2 g of WS_2 nanopowder was ground and added to 20 ml of 35% ethanol solution. The sol is then sealed in a closed vial and subjected to ultrasonication (50 kHz), for nearly 120 min. The supernatant is collected in an eppendorf after the sol was subjected to centrifugation (~1500 rpm), for 10 min. This was centrifuged (~3500 rpm) further for a time duration of 30 min. Subsequently, the resulting supernatant is carefully removed and kept as the finished product.

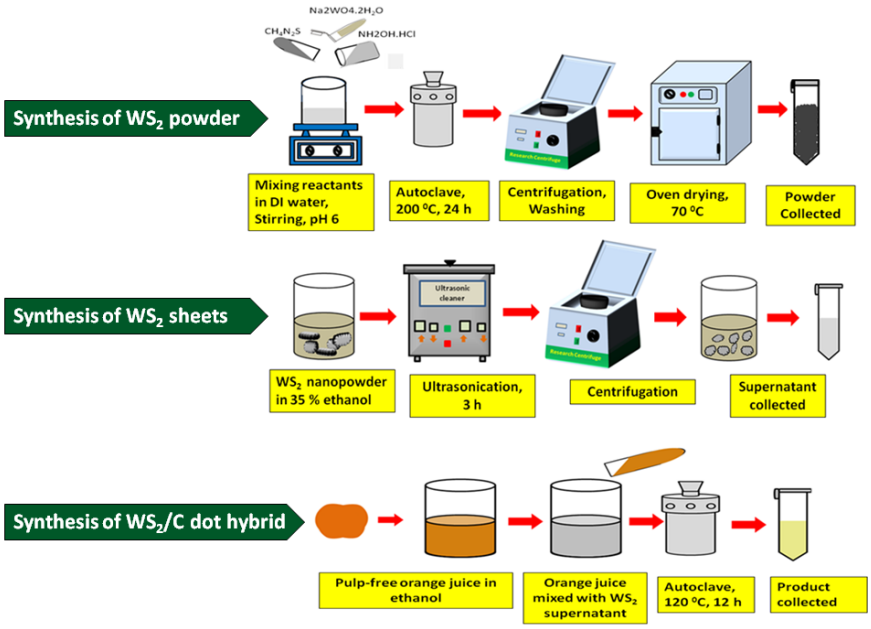

Figure 2.16: Schematic block diagram of the synthesis steps for processing WS_2 nanopowder, nanosheets and WS_2/C-dot hybrid nanosystems.

Following an earlier work [35], in a typical process, 20 ml of matured orange juice (absolutely pulp-free) was mixed with 15 ml ethanol in a beaker. First, a mixture of 10 ml of the as collected WS_2 supernatant and 10 ml of the clean orange juice was transferred into a 50 ml teflon lined stainless-steel autoclave. After sealing airtight, the autoclave was subjected to heating at a constant temperature of 120 °C, for about 2 h. After the reaction is over, the autoclave was allowed to cool down naturally. As a result, a yellowish coloured sol is obtained, which exhibited bluish green fluorescence under UV excitation. A schematic block diagram illustrating synthesis steps can be found in Fig. 2.16.

2.4.2 Structural and morphological analyses

Fig. 2.17 (a) depicts powder x-ray diffractogram (XRD) of the synthesized WS_2 nanosheets. As can be noticed, the most intense diffraction peak is located at the Bragg's angle, $2\theta = 14.40°$, which corresponds to the (002) plane of the hexagonal WS_2. The other diffraction peaks at ~28.87°, 32.58°, 33.41°, 35.97°, 39.49°, 44.75°, 49.80°, 55.36° are attributed to the respective crystallographic planes indexed as, (004), (100), (101), (102), (103), (006), (105) and (106) of the hexagonal WS_2 system (JCPDS File No. 08 0237) [8].

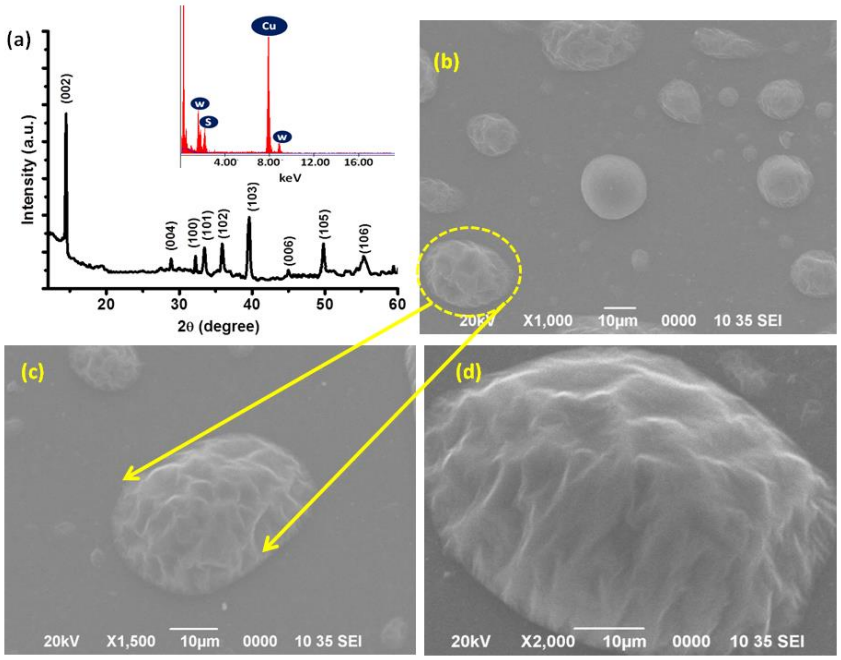

Figure 2.17: (a) X-ray diffractogram and (b-d) scanning electron micrographs of the synthesized nano-WS_2 system. Note the sheets with folds and kinks at higher magnifications. The EDX spectrum is shown as inset in (a).

Fig. 2.17 (b-d) essentially characterizes a set of the SEM micrographs of the WS_2 nanosheets, captured at low and high magnifications. Several folds and kinks can be clearly witnessed in the WS_2 nanosheets. The elemental composition is ascertained from the EDX spectrum of the WS_2 nanosystem, shown as inset of Fig. 2.17 (a). The presence of W and S elements is quite evident from the spectrum along with the Cu peak that might have arisen from the Cu-grid normally used to hold the specimen under study.

Fig. 2.18 (a-c) shows a series of TEM micrographs of the as prepared 2D WS_2/C-dot nanohybrid system captured in order of increasing magnifications. Apparently, nearly spherical C-dots with size varying in the range of 2 to 5 nm were observed to spread over the nanosheets of WS_2 (Fig. 2.18 (a-c)). Moreover, the lattice fringe patterns of both the systems could be revealed at higher magnifications (Fig. 2.18 (d, e)). The respective interplanar (d-) spacings of the

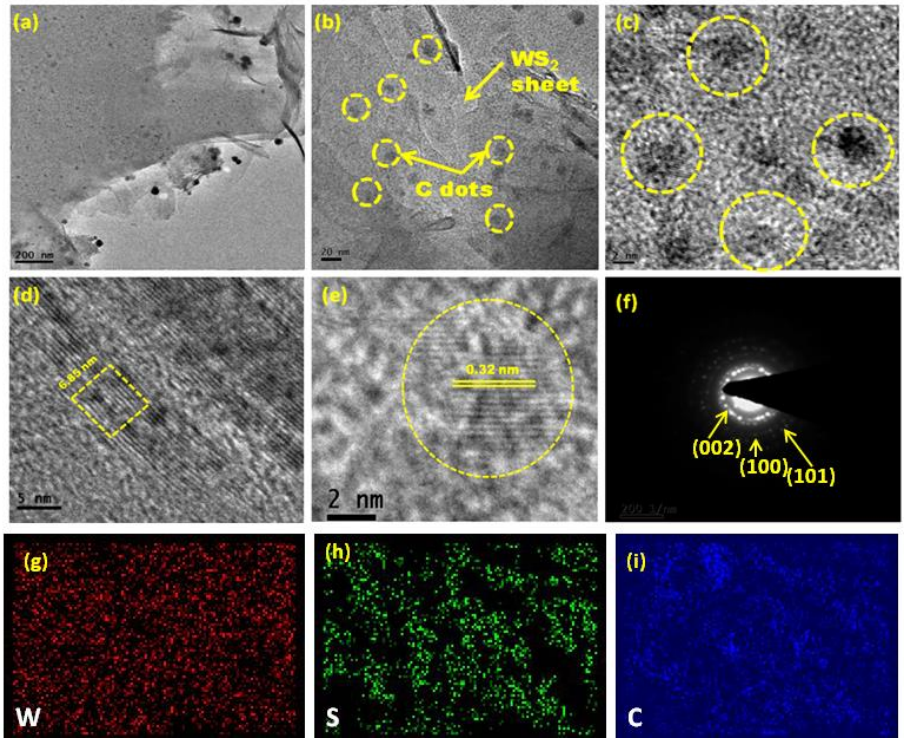

Figure 2.18: TEM images of (a) nano-WS_2 with C-dots at low magnification, (b) WS_2/C-dot nanohybrid at a higher magnification, and (c) an enlarged view of the isolated C-dots. Information with regard to lattice fringe patterns of the WS_2 and C-dot systems can be noticed in (d) and (e); respectively. The SAED pattern highlighting diffused rings is shown in (f). Whereas, elemental mappings of the WS_2/C-dot nanohybrid can be found in (g-i).

WS_2 nanosheet, and C-dots, as measured with the help of using *ImageJ*® software are approximately, 0.62 nm and 0.34 nm. The C-dots are, infact, fairly uniform in size and were seen to spread all over the 2D plane of the WS_2 nanosheets, without being agglomerated. The diffused rings, found in the SAED pattern indicate polycrystalline nature of the specimen under study (Fig. 2.18 (f)). The images which illustrate elemental mapping of the WS_2/C-dot nanohybrid are depicted in Fig. 2.18 (g-i). It essentially illustrates the visual evidence of distribution of relevant elements W, S and C present in the system. The elemental signals were generated independently in a specific area and then, assigned with a distinct colour pattern for the sake of clarity and comparison purposes.

2.4.3 Characteristic growth mechanism

The formation of WS_2 nanopowder by the hydrothermal process involves the following reaction steps [36]:

$$Na_2WO_4\ (s) + 4CH_4N_2S\ (s) + 4H_2O\ (l) \rightarrow 4CO_2\ (g) + Na_2WS_4\ (s) + 8NH_3\ (g)$$

$$Na_2WS_4(s) + 2NH_2OH.HCl(s) \rightarrow WS_2(s) + N_2(g) + 2H_2O(l) + 2H_2S(g) + 2NaCl(s)$$

In the first step, Na_2WO_4 reacts with CH_4N_2S to form Na_2WS_4. Then in the next step, Na_2WS_4 is reduced to WS_2 in presence of the reducing agent NH_2OH. HCl [37] . Thus, nucleation and subsequent aggregation takes place in order to minimize the overall surface energy of the system. In absence of any surfactants in the reaction process, the morphology of the WS_2 appears in the form of thin sheets. Owing to the lowered surface energy along the [0001] direction, the preferred growth direction of the WS_2 crystal is along the c-axis [40]. Subsequently, the WS_2 sheets tend to aggregate along the c-axis and eventually end up with stacks of WS_2 sheets [38].

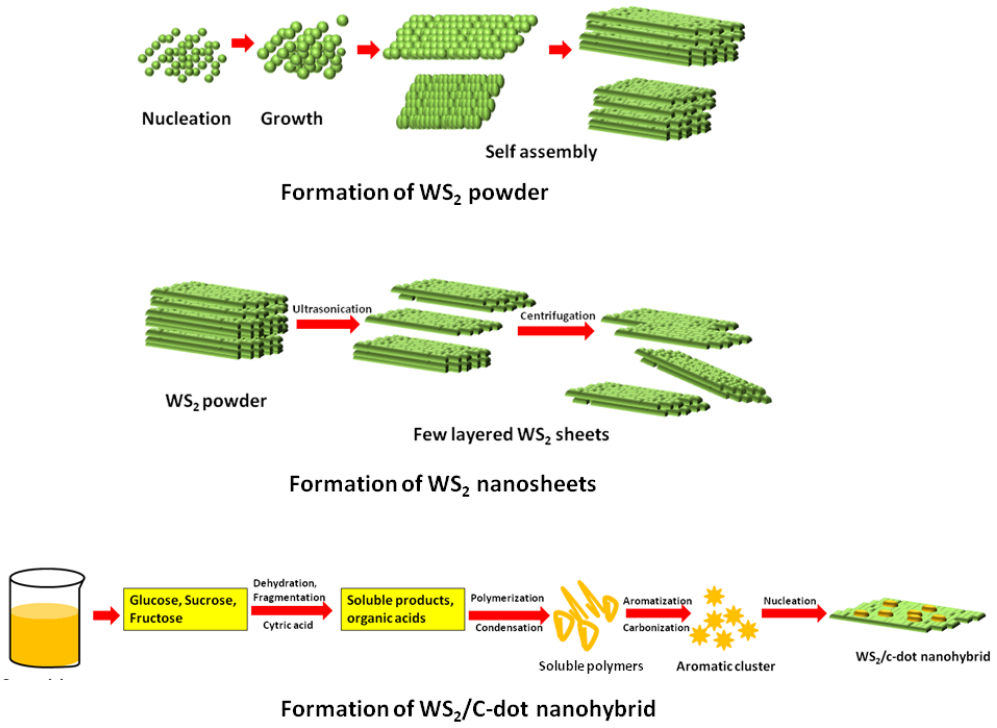

Figure 2.19: Schematic figure representing the growth mechanism of the nanosheets and nano hybrid systems.

The bulk WS_2 nanopowder is then dissolved in 35% ethanol solution and ultrasonicated for 120 min. The highly intense ultrasound waves helps to peel out few layer nanosheet out of the bulk powder. The few layered WS_2 nanosheets were obtained by taking the supernatant after a series of centrifugation.

The mechanism of formation of carbon dots from the orange juice by the hydrothermal process is not clear yet [35]. However, it is believed that carbon dots are formed by the hydrothermal carbonization of the constituents of orange juice. Sucrose that found in orange juice when hydrothermally treated gives rise to the formation of glucose and fructose [35]. The dehydration and decomposition of the glucose/fructose result in the formation of several soluble compounds and organic acids. Citric acid present in the orange juice plays an important role in the dehydration and decomposition processes by allowing the reaction to happen in a controlled manner. The polymerisation and condensation of these products gave rise to soluble polymers. Consequently, aromatization and carbonization of these soluble polymers led to the formation of aromatic clusters [35]. When concentration of aromatic clusters reaches a critical supersaturation point, nucleation takes place abruptly and carbon dots are formed eventually on the WS_2 surface.. From the TEM micrographs, one could clearly visualize surface anchored c-dots depicted in Fig. 2.18.

2.5 Conclusion

We have demonstrated a user friendly synthesis of IF-type WS_2 nanoparticles. The hexagonal crystal structure of WS_2 is evident from the XRD analysis. The presence of elements W and S has been confirmed from the EDX spectrum. The direct band gap of nano-WS_2, as predicted from the Tauc's plot is ~1.91 eV. The single distinct peak located at 630 nm corresponds to the indirect-to-direct band gap type transitions. On the other hand, Raman spectrum reveals the presence of one in-plane E^1_{2g} mode and one A_{1g} out of plane mode. The formation of IF-type nanoparticles with an average outer diameter of 16 nm has been predicted

through the electron micrographs. We have demonstrated spectroscopic and sorption characteristics of the WS_2 nanosheets derived through a hydrothermal route and exfoliation. While possessing a hexagonal crystal structure, the nanosheets exhibited a lattice spacing of 0.63 nm. Raman measurement on the WS_2 nanosheets has revealed E^1_{2g} and A_{1g} modes with an intensity ratio of ~0.68, which is higher than its value for the bulk counterpart. The BET N_2 adsorption-desorption curve gives a type-IV pattern with an open hysteresis feature. Exhibiting a high surface area, the nanosheets are believed to have mesopores with an average pore dimension of ~3.8 nm. Hydrothermally synthesized 2D WS_2 nanosheets, decorated with C-dots have also been processed and characterized. The TEM images have revealed the formation of 2-5 nm sized C-dots, that are found to spread over the surfaces of WS_2 nanosheets.

References

[1] Pol, V.G., Pol, S.V., George, P.P., Gedanken, A. Combining MoS_2 or $MoSe_2$ nanoflakes with carbon by reacting $Mo(CO)_6$ with S or Se under their autogenic pressure at elevated temperature. *Journal of Material Science*, 43:1966–73, 2008.

[2] Ellmer, K., Mientus, R., Seeger, S., Weiβ, V. Highly (001)-textured WS_{2-x} films prepared by reactive radio frequency magnetron sputtering. *Physica Status Solidi A*, 201:R97–R100, 2004.

[3] Hu, J.J., Zabinski, J.S., Sanders, J.H., Bultman, J.E., Voevodin, A.A. Pulsed Laser Syntheses of Layer-Structured WS_2 Nanomaterials in Water. *Journal of Physical Chemistry B*, 110: 8914–6. 2006;

[4] Shang, Y., Xia, J. Xu, Z., Chen, W. Hydrothermal synthesis and characterization of quasi 1D tungsten disulfide nanocrystal.

[5] Park, S.W., Jang, J.T., Cheon, J., Lee, H.H., Lee, D.R., Lee, Y. Shape dependent compressibility of TiO_2 anatase nanoparticles. *Journal of Physical Chemistry C*, 112(26):9627–9631, 2008.

[6] Hazarika, S., Mohanta, D. Extraction and characterization of mixed phase KNO_2–KNO_3 nanocrystals derived from flat-leaf green spinach. *Physica Scrpta*, 87:015603-1–5, 2013.

[7] Garcı´a-Lecina, E. I., Garcı´a-Urrutia, Dı´ez, J.A., Fornell, J., Pellicer, E., Sort, J. Codeposition of inorganic fullerene-like WS_2 nanoparticles in an electrodeposited nickel matrix under the influence of ultrasonic agitation. *Electrochimica Acta*, 114:859–867, 2013.

[8] Cao, S., Liu, T., Hussain, S., Zeng, W., Peng, X., Pan, F. Hydrothermal synthesis of variety low dimensional WS_2 nanostructures. *Materials Letters*, 129:205–208, 2014.

[9] Elechiguerra, J.L., Reyes-Gasga, J., Jose-Yacaman, M. The role of twinning in shape evolution of anisotropic noble metal nanostructure. *Journal of Material Chemistry*, 16:3906–3919, 2006.

[10] Zhang, Y., Zhang, Y., Ji, Q., Ju, J., Yuan, H., Shi, J., Gao, T., Ma, D., Liu, M., Chen, Y., Song, X., Hwang, H.Y., Cui, Y., Liu, Z. Controlled growth of high-quality monolayer WS2 layers on sapphire and imaging its grain boundary. *ACS Nano*, 7:8963–8971, 2013.

[11] Schuffenhauer, C., Popovitz-Biro, R., Tenne, R. Synthesis of NbS_2 nanoparticles with (nested) fullerene-like structure (IF). *Journal of Material Chemistry*, 12:1587–1591, 2002.

[12] Zeng, H., Liu, G-B., Dai, J., Yan, Y., Zhu, B., He, R., Xie, L., Xu, S., Chen, X., Yao, W., Cui, X. Optical signature of symmetry variations and spin-valley coupling in atomically thin tungsten dichalcogenides. *Scientific Reports*, 3:1608, 2013.

[13] Atkin, P., Daeneke, T., Wang, Y., Carey, B.J., Berean, K.J., Clark, R.M., Ou, J.Z., Trinchi, A., Cole, I.S., Kalantar-zadeh, K. 2D WS_2/carbon dot hybrids with enhanced photocatalytic activity. *Journal of Material Chemistry A*, 4:13563–13571, 2016.

[14] Gutierrez, H.R., Perea-Lopez, N., Elias, A.L., Berkdemir, A., Wang, B., Lv, R., Lopez-Urias, F., Crespi, V.H., Terrones, H., Terrones, M. Extraordinary

room-temperature photoluminescence in triangular WS_2 monolayers. Nano Letters, 13:3447–3454, 2013.

[15] Berkdemir, A., Gutie´rrez, H.R., Botello-Me´ndez, A.R., Perea- Lo´pez, N., Elı´as, A.L., Chia, C.I., Wang, B., Crespi, V.H., Lo´pez-Urı´as, F., Charlier, J.C., Terrones, H., Terrones, M. Identification of individual and few layers of WS_2 using Raman spectroscopy. *Scientific Reports*, 3:1755, 2013.

[16] Coates, J. Interpretation of infrared spectra, a practical approach in encyclopedia of analytical chemistry, ed. R.A. Meyers (Wiley,Chichester, 2000), p. 10829.

[17] Vattikuti, S.V.P., Byon, C. Effect of CTAB surfactant on textural, structural, and photocatalytic properties of mesoporous WS_2. *Science of Advanced Materials*, 7(12):2639–2645, 2015.

[18] Feldman, Y., Frey, G.L., Homyonfer, M., Lyakhovitskaya, V., Margulis, L., Cohen, H., Hodes, G., Hutchison, J.L., Tenne, R. Bulk synthesis of inorganic fullerene-like MS_2 (M = Mo, W) from the respective trioxides and the reaction mechanism. *Journal of American Chemical Society*, 118:5362–5367, 1996.

[19] Frey, G.L., Elani, S., Homyonfer, M., Feldman, Y., Tenne, R. Optical-absorption spectra of inorganic fullerene like MS_2 (M=Mo, W). *Physical Review B*, 57:6666-6671, 1998.

[20] Notley, S.M. High yield production of photoluminescent tungsten disulphide nanoparticles. *The Journal of Colloid and Interface Science*, 396:160–164, 2013.

[21] Sang, Y., Zhao, Z., Zhao, M., Hao, P., Leng, Y., Liu, H. From UV to near-infrared, WS_2 nanosheet: a novel photocatalyst for full solar light spectrum photodegradation. *Advanced Materials*, 27:363–369, 2015.

[22] Parshetti, G., Kalme, S., Saratale, G., Govindwar, S. Biodegradation of Malachite Green by Kocuria rosea MTCC 1532. *Acta Chimica Slovenica*, 53:492–498, 2006.

[23] Mao, X., Xu, Y., Xue, Q., Wang, W., Gao, D. Ferromagnetism in exfoliated tungsten disulfide nanosheets. *Nanoscale Research Letters*, 8:430, 2013.

[24] Lin, H., Wang, J., Luo, Q., Peng, H., Luo, C., Qi, R., Huang, R., Travas-Sejdic. J., Duan, C-G. Rapid and highly efficient chemical exfoliation of layered MoS_2 and WS_2, *Journal of Alloys and Compounds,* 699:222-229, 2017.

[25] http://imagej.nih.gov/ij/

[26] Ghorai, A., Bayan, S., Gogurla, N., Midya, A., Ray, S. K. Highly luminescent WS_2 quantum dots/ZnO heterojunctions for light emitting devices. *ACS Applied Material Interfaces*, 9:558, 2017.

[27] Nguyen, T. P., Choi, S., Jeon, J-M., Kwon, K. C., Jang, H.W., Kim, S. Y. Transition Metal Disulfide Nanosheets Synthesized by Facile Sonication Method for the Hydrogen Evolution Reaction. *Journal of Physical Chemistry C*, 120:3929, 2016.

[28] Nguyen, T. P., Sohn, W., Oh, J. H., Jang, H. W. Kim, S. Y. Size-Dependent Properties of Two-Dimensional MoS_2 and WS_2. *Journal of Physical Chemistry C*, 120:10078, 2016.

[29] Molina-Sanchez, A., Wirtz, L. Phonons in single-layer and few-layer MoS_2 and WS_2. *Physical Review B: Condensed Matter*, 84**:**155413-1-8, 2011.

[30] Le Q. V., Nguyen T. P., Kim, S. Y. UV/ozone-treated WS_2 hole-extraction layer in organic photovoltaic cells, *Physica status solidi (RRL)–Rapid Research Letters*, 8:390-394, 2014.

[31] Berkdemir, A., Gutiérrez, H.R., Botello-Méndez, Andrés, R., Perea- López, N., Elías, Ana, L., Chia, C-I., Wang, B., Crespi, V. H., Lo´pez-Urı´as, F., Charlier, J-C., Terrones, H. Identification of individual and few layers of WS_2 using Raman Spectroscopy. *Scientific Reports*, 3:1755, 2013.

[32] Alothman, Z. A. A Review: Fundamental Aspects of Silicate Mesoporous Materials. *Materials*, 5:2874-2902, 2012.

[33] Kruk, M., Jaroniec, M. Gas Adsorption Characterization of Ordered Organic−Inorganic Nanocomposite Materials. *Chemistry of Materials,* 13:316, 2001.

[34] Butt H-J., Graf, K., Kappl, M. *The Kelvin equation: physics and chemistry of interfaces*. Weinheim: Wiley-VCH, 2006.

[35] Sahu, S., Behera, B., Maiti, T.K., Mohapatra, S. Simple one-step synthesis of highly luminescent carbon dots from orange juice: application as excellent bio-imaging agents, *Chemical Communications*, 48: 8835-8837, 2012.

[36] Lin, H.T., Chen, X.Y., Li, H.L., Yang, M., Qi, Y.X. Hydrothermal synthesis and characterization of MoS_2 nanorods, *Materials Letters*, 64:1748–50, 2010.

[37] Tang, G., Tang, H., Li, C., Li, W., Ji, X. Surfactant-assisted hydrothermal synthesis and characterization of WS_2 nanorods. *Materials Letters*, 65: 3457–3460, 2011.

[38] Cao, S., Zhao, C., Peng, L., Han, T. Synthesis of uniform WS_2 nanoflowers via a sodium silicate-assisted hydrothermal process. *Journal of Material Science: Mater Electron*, 27:3821–3825, 2016.